An Automated COMSOL and Optuna Workflow for Pixelated Optical Structures

Xinxiang Ye[1], Qiyue Chen[1], Kaichen Dong[1*]
1. Shenzhen International Graduate School, Tsinghua University, Shenzhen, China
Xinxiang Ye: yxx24@mails.tsinghua.edu.cn
Qiyue Chen: chenqy23@mails.tsinghua.edu.cn
* Corresponding author: Kaichen Dong, dkc22@sz.tsinghua.edu.cn

Abstract
We present an automated COMSOL and Optuna workflow for pixelated Au/Cr/SiO_2 structures on a semi-infinite Si substrate. Python and LiveLink for MATLAB coordinate model preparation, full-wave batch solution, power extraction and persistent storage. Run-level checks verify wavelengths, finite outputs and power consistency before recording a discrete absorptance objective at 21 wavelengths from 8 to 13 μm under normally incident x-polarized illumination. Numerical acceptance is assessed separately. An opaque planar reference agrees with an independent transfer-matrix solution with a maximum relative absorptance error of 0.00568%; a transmitting reference verifies transmitted-power extraction. Three baselines and six search evaluations, including one startup sample, demonstrate the loop. Source reconstruction and a baseline replay through the corrected controller reproduce the archived response on the same machine. No search candidate exceeds the initial or empty-window baseline, and patterned spectra fail mesh and perfectly matched layer (PML) acceptance criteria. The study illustrates how traceability and separate numerical checks support the interpretation of automated simulations.
Keywords: periodic optical structure; COMSOL Multiphysics; automated simulation; optical absorption; computational provenance.

1. Introduction

Exploring pixelated periodic structures requires repeated electromagnetic evaluations with consistent model updates, spectral extraction and result storage. We integrate binary design variables, geometric screening, full-wave simulation and sequential candidate selection into an automated workflow, assessed through uniform-layer references, batch evaluations and repeated calculations.

Photonic inverse design includes fabrication-constrained design and topology optimization [1,2]. Large-area metasurface optimization can treat each pixel as a design variable [2], and Bayesian optimization has been coupled to COMSOL for frequency-selective mantle-cloak metasurfaces [3]. Here, we address the complementary task of tracing evaluations and screening outputs before recording exploratory objectives. Reference comparisons and mesh/PML sensitivity tests separately assess accuracy. Random search provides a useful control for model-based search when only a subset of variables determines performance [4].

Computational provenance links inputs, software operations and outputs to support interpretation and reproduction [5]. Finite-element studies of diffraction gratings also show that mesh error and PML truncation must be assessed together [6]. We therefore distinguish execution completion, run-level screening and numerical acceptance, with same-machine repeatability as an additional check on model reconstruction and result extraction.

The contributions are a persistent Python–MATLAB–COMSOL loop linking designs to models, spectra, objectives and logs; separate run-level screening and numerical acceptance; and identification of a duplicate-handling defect from the stored history. These mechanisms provide a basis for tracing and replaying other parameterized simulation studies.

The test structure comprises patterned Au/Cr/SiO_2 layers, a continuous SiO_2 spacer and a semi-infinite Si substrate, with no metallic back reflector. Material substitution in an existing geometry retained its layer thicknesses and surrounding frame. Only the binary pixel occupancies vary.

2. Design representation and objective

A 6×6 binary matrix defines the 36 design variables. Each pixel contains three prepartitioned layer domains assigned either the Au/Cr/SiO_2 stack or air. The surrounding frame and continuous lower layers remain fixed within the modeled unit cell. The reported search requires every four-connected component of occupied pixels to reach a matrix edge. This geometric rule was inherited from a suspended structure and is optional in the corrected evaluator because the present stack has a continuous supporting spacer. The matrix-to-domain mapping was checked at all 36 pixel centers: row indices increase along y, column

indices increase along x, and MATLAB's column-major ordering selects the corresponding material domains.

Table 1 summarizes the geometry and optical-data sources. The fixed frame covers 58.7% of the unit-cell area. The 50 nm computational Si region represents part of the semi-infinite substrate rather than a separate film or back reflector. A Si buffer and lower PML represent the substrate continuation in the patterned model.

Table 1. Fixed geometry and material sources.

Component	Size	Material or specification
Cell / window	28 / 18 µm	Square
Pixel / frame width	3 / 5 µm	6×6 binary window
Top pixel layer	95 nm	Au, Olmon et al. [7]
Middle pixel layer	36 nm	Cr, Rakić et al. [8]
Lower pixel layer	160 nm	SiO_2, Kischkat et al. [9]
Continuous spacer	1 µm	SiO_2, same source
Substrate	Semi-infinite	Si, Chandler-Horowitz and Amirtharaj [10]

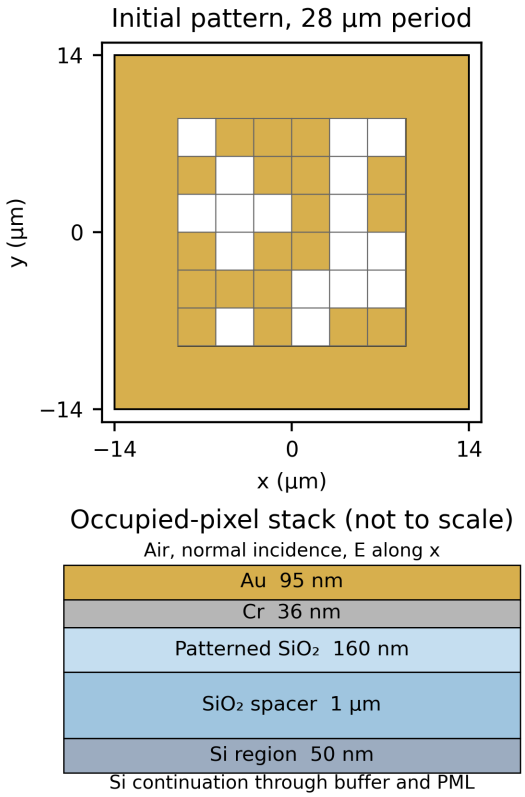


Figure 1. Initial pattern with 19 occupied pixels and the layer stack in an occupied pixel. Gold denotes occupied pixels and the fixed frame; white denotes air-filled pixels. Layer thicknesses are not to scale.

The objective is the discrete Planck-weighted average absorptance

$$J = \frac{\Sigma_i A_x(\lambda_i) B\lambda(\lambda_i, Tw)}{\Sigma_i B\lambda(\lambda_i, Tw)}$$

$\lambda_i = 8 + 0.25(i - 1)$ µm; i = 1,…,21; Tw = 282.15 K. Here $B\lambda = 2hc^2 / \{\lambda^5[\exp(hc/(\lambda k B Tw)) - 1]\}$. To reproduce the archived objectives, the implementation retains $h = 6.626\times10^{-34}$ J·s, $c = 3.0\times10^8$ m/s and $k_B = 1.38\times10^{-23}$ J/K, with λ in metres. The inherited value of 282.15 K defines the spectral weighting and does not represent a device temperature. All baseline and search evaluations use the same 21 wavelengths, with no additional endpoint factors in the discrete sum. The spectral weights vary by a factor of 1.18 across the band. For the ten archived designs, the weighted mean differs from the arithmetic mean by at most 0.61% relative. J therefore provides a consistent scalar objective for normally incident x-polarized illumination, with modest sensitivity to the chosen weighting.

3. COMSOL model and numerical verification

The model uses COMSOL Multiphysics 6.2 with the Wave Optics Module, the Electromagnetic Waves, Frequency Domain interface (ewfd) and LiveLink™ for MATLAB® [11]. For linear, nonmagnetic materials under COMSOL's time-harmonic convention, the source-free electric field satisfies

$$\nabla \times (\mu_r^{-1} \nabla \times E) - k_0^2 \varepsilon_r E = 0$$

The dispersive refractive index and extinction coefficient are linearly interpolated from the material tables cited in Table 1 and accessed through refractiveindex.info [12]. The database entries are Olmon-ev.yml for Au (evaporated gold), Rakic-LD.yml for Cr, Kischkat.yml for SiO_2 and Chandler-Horowitz.yml for Si. These data describe reference samples or dispersion models. For Cr, the Lorentz–Drude model of Rakić et al. [8] has a reported range extending to approximately 12.4 µm, whereas the tabulated values used here extend to 13 µm. The long-wavelength results must therefore be interpreted within this material-model limitation. Floquet periodic conditions are imposed on the lateral boundaries. Normally incident x-polarized excitation is normalized to 1 W per full unit cell. The uniform reference uses periodic ports, whereas the patterned model uses an interior slit periodic port with domain-backed excitation and upper and lower PMLs [11,13]. The search used rational PMLs; subsequent diagnostics used polynomial PMLs. The symmetric empty-window half-cell uses perfect electric conductor boundaries on the x faces, periodicity along y and 0.5 W incident power. This symmetry reduction is not applicable to arbitrary patterns.

The 28 µm period exceeds all free-space wavelengths considered (P/λ = 2.15–3.5), so the structure supports multiple diffraction orders. Air-

side orders reach |m| = 3 at the short-wavelength end, with Rayleigh thresholds at 8.854, 9.333, 9.899 and 12.522 μm. More orders can propagate in Si. Full-cell flux integrals include the diffracted power represented in the field solution; single-mode S-parameters alone would be insufficient.

For the patterned PML models, let S_z = ewfd.Poavz denote the time-averaged z-directed Poynting flux of the solved field. The extraction uses $R = \int S_z \, dS/P_{in}$ on the air monitor above the downward-launching slit port, and $T = -\int S_z \, dS/P_{in}$ at the bottom of the original 50 nm Si region. In the standard configuration, the air monitor lies halfway through the added 3 μm air buffer, 1.5 μm above the port; the transmission monitor precedes the added Si buffer. Above the slit, the source does not launch an incident wave, so the reflection integral requires neither incident-power subtraction nor an explicit reflected-field decomposition. Residual PML reflections can affect these net fluxes and are tested separately. Absorptance A integrates ewfd.Qh over the pixel and frame layers, continuous spacer and original Si region, divided by P_{in}. PML and added-buffer losses are excluded; transmitted power includes energy subsequently absorbed deeper in Si.

The baseline and search models use a swept mesh with a maximum lateral element size of 1.5 μm, five elements through each physical domain and ten layers in each rational PML. The initial-pattern model contains 27,520 hexahedral elements and 690,616 degrees of freedom, with a second-order electric-field approximation. The direct MUMPS solver uses out-of-core storage with an in-core allocation of 8192 MB. At this mesh setting, a 3 μm pixel spans approximately two lateral elements, while $\lambda/\mathrm{Re}(n_{Si})$ is approximately 2.34 μm at a free-space wavelength of 8 μm. Section 5.3 assesses the sensitivity to discretization.

Subsequent boundary diagnostics used polynomial PMLs with 20 layers, curvature 3 and scaling factor 1. The reference air and Si buffers were 3 and 2 μm thick, respectively, and each PML was 3 μm thick. Flux monitors remained on physical planes, with 0.05 μm guard regions resolved by five swept elements. Run-level power screening required $|R+T+A-1| \le 0.001$ and $|(1-R-T)-A|/\max(|A|,10^{-12}) \le 1\%$. These are absolute and relative measures of the same residual, with A independently calculated from volume loss. Separate mesh/PML comparisons required $|A_{cmp}-A_{base}|/\max(|A_{cmp}|,10^{-12}) \le 1\%$ and $|\Delta R|, |\Delta T| \le 0.001$ at matching wavelengths. Here base is the first input and cmp is the second input, evaluated with the changed settings; the reported relative changes use this convention. Section 5.1 specifies the uniform-reference thresholds.

4. Optimization workflow

Python calls MATLAB through MATLAB Engine, and MATLAB controls COMSOL through LiveLink for MATLAB. Optuna's tree-structured Parzen estimator (TPE) [14,15,16] selects candidates by fitting density estimates to accumulated evaluations. The six-evaluation campaign demonstrates this automated loop.

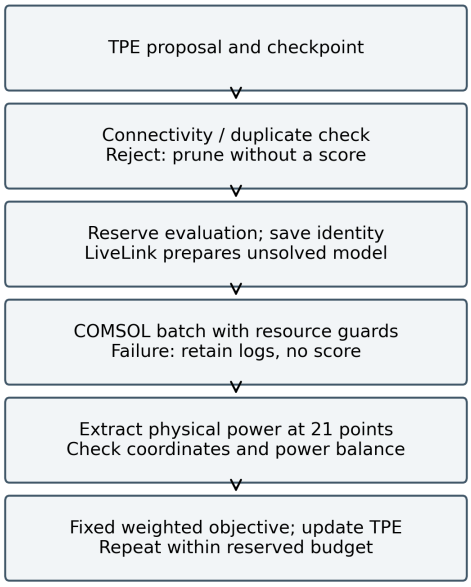


Figure 2. Workflow of the archived controller used for the six-evaluation study. The corrected controller replaces duplicate pruning with verified cached values. Mesh/PML acceptance is assessed separately from the run-level checks shown here.

For each evaluation, LiveLink prepares an input model, Python launches the native COMSOL batch solver, and LiveLink reads the saved solution. Execution is complete when model preparation, solution and extraction succeed. Run-level checks verify wavelengths, finite outputs and power consistency before recording the objective. Numerical acceptance is assessed separately through reference comparisons and mesh/PML sensitivity tests. The archived patterned objectives remain in the optimization history as exploratory data despite failed accuracy checks. Model hashes, requested wavelengths, solver logs and resource measurements preserve the context of each result.

The archived evaluator used a persistent Optuna 4.1.0 TPE study with seed 42 and n_startup_trials = 4. The budget allowed six full-wave evaluations and at most 64 suggestions. Preparation and solver failures counted toward the evaluation budget; disconnected and duplicate patterns were pruned without an objective value or solver call. Each invocation evaluated at most one feasible candidate using 24 CPU cores and a 3600 s solver time limit. Optuna counts both completed and pruned trials toward startup, and only one successful physical evaluation preceded model-guided sampling in this history. Nine duplicate suggestions were recorded as PRUNED without intermediate values and entered TPE's upper (unfavorable) group, distorting the observations used for sampling. The default

sampler modeled bits independently, and baseline results were not supplied to the sampler. The duplicate-handling defect and these sampling limitations preclude conclusions about TPE performance.

The study is stored in SQLite, with a checkpoint for the pending candidate. Model, code, settings and spectrum hashes accompany each stored matrix and result to support traceable local replay. The supplementary reproducibility note provides a worked empty-window record linking the candidate and settings to model and spectrum hashes, screening status, objective and execution log.

The corrected controller preserves the original study as a separate record. It returns verified cached objectives for duplicate candidates and records rejections under the optional connectivity rule as FAIL without an objective value. Empty, initial and solid patterns are queued as baselines. The software also supports serial evaluation with a fixed budget, random sampling and multivariate TPE. Its behavior is covered by seventeen regression tests. A queued 21-point empty-window evaluation completed the full workflow, from model preparation to persistent study update. Section 5.2 reports the archived six-pattern search, and Section 5.3 reports the replay through the corrected controller.

5. Validation design and results

5.1 Uniform-layer verification

Assigning the occupied stack to all pixels produces a uniform Au/Cr/SiO_2/Si structure. For this planar reference only, the transverse period was set to 1 µm without changing the physical layers or optical data. The stack admits an independent transfer-matrix solution at normal incidence: air/Au (95 nm)/Cr (36 nm)/SiO_2 (1160 nm)/Si (50 nm), terminated by semi-infinite Si.

The reference was evaluated at all 21 wavelengths using a swept mesh with ten elements through each physical domain. A_{port} denotes COMSOL's total absorptance variable, ewfd.Atotal, and A_{vol} denotes the integral of ewfd.Qh over the computational domains normalized by incident power. Their maximum absolute difference was 3.83×10^{-15}. The separate field-flux residual, $\varepsilon_{flux} = |P_{upper} + P_{lower} + Q_{vol}|/P_{in}$, uses independently integrated outward Poynting fluxes at the upper and lower boundaries and total volume dissipation Q_{vol}. Its maximum was 4.27×10^{-5}. These metrics use different power extractions and need not yield identical residuals.

The maximum relative error in A_{port} against the transfer-matrix solution was 0.00552%. The weighted absorptance was 0.0096792 in COMSOL and 0.0096788 in the reference. All three declared criteria were met: relative A error ≤1%, $|A_{port}-A_{vol}| \le 10^{-8}$ and $\varepsilon_{flux} \le 10^{-4}$.

The 21-point batch required approximately 125 s on an Intel Core i9-13900HX with 24 allocated CPU cores, including model loading and saving. The solver reported a peak physical memory use of approximately 3.88 GB. Agreement with the independent reference verifies the material interpolation, uniform-layer response, power extraction and objective calculation for this case.

A separate planar reference with PMLs tested the boundary treatment used in subsequent models at the same 21 wavelengths. With 30 swept elements per PML, scaling factor 1 and vertical air-mesh spacing ≤25 nm adjacent to the reflection monitor, the maximum relative absorptance error was 0.00568%. Maximum absolute errors in R and T were 3.14×10^{-5} and 1.33×10^{-10}, respectively, and the maximum $|R+T+A-1|$ was 3.19×10^{-5}. All criteria were met: relative A error ≤1%, and absolute R error, absolute T error and power residual each $\le10^{-4}$. The model contained 277,738 degrees of freedom and required approximately 276 s.

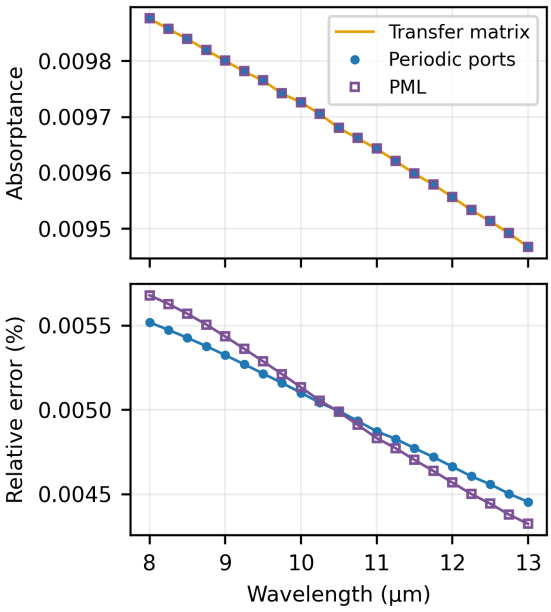


Figure 3. Absorptance spectra of the opaque uniform stack and relative errors against the independent transfer-matrix reference for periodic-port and PML models.

Because $T \approx 10^{-7}$ for the opaque stack, the comparison primarily tests R and A. A transmitting reference was obtained by removing the metal layers, giving air/SiO_2 (1160 nm)/Si (50 nm)/Si half-space with the same 1 µm period. The transfer-matrix transmittance ranged from 0.0339 to 0.9104 over the 21 wavelengths. Acceptance required relative A and T errors ≤1%, absolute R and T errors ≤0.001, and the run-level power criteria in Section 3. With ten lower-PML layers, the maximum absolute T error and power residual were both 1.50×10^{-3} and exceeded their limits. Increasing only the lower PML to 40 layers reduced these values to 9.44×10^{-5} and 9.48×10^{-5}, respectively; the maximum relative T error was 0.0111%. The 40-layer model met all criteria, verifying transmitted-power extraction for the

uniform reference and demonstrating sensitivity to lower-PML discretization.

Table 2. Verification and sensitivity checks with limits for the reported metrics. Pass denotes satisfaction of all applicable criteria in Sections 3 and 5.1. Patterned comparisons apply only to the tested wavelengths.

Check	Metric and value	Limit	Result
Opaque stack, ports	Relative A: 0.00552%	1%	Pass
Opaque stack, PML	Relative A: 0.00568%	1%	Pass
Transmitting stack, 10 lower PML layers	Absolute T: 1.50×10^{-3}	0.001	Fail
Transmitting stack, 40 lower PML layers	Absolute T: 9.44×10^{-5}	0.001	Pass
Initial pattern, h = 1.0 → 0.75 µm at 10.5 µm	Absolute R: 1.77×10^{-3}	0.001	Fail
Empty window, rational PML factor 1 → 2, four wavelengths	Absolute R: 3.57×10^{-3}	0.001	Fail
Empty window, polynomial PML 40 → 20 layers at 13 µm	Absolute R: 1.33×10^{-5}	0.001	Pass
Empty half-cell, h = 1.0 → 0.9 µm, four wavelengths	Absolute R: 8.50×10^{-4}	0.001	Pass

5.2 Baseline evaluations and bounded search

Three baselines were evaluated at all 21 wavelengths using the same 28 µm unit cell, h = 1.5 µm lateral mesh and ten-layer rational PMLs. The initial pattern with 19 occupied pixels, empty variable window and solid window yielded J = 0.0813, 0.1051 and 0.00969, respectively. The empty-window model retains the surrounding frame and continuous lower layers. The corresponding batch runtimes were approximately 1731, 1727 and 2260 s, with maximum normalized power-balance residuals of 7.95×10^{-6}, 1.47×10^{-5} and 5.15×10^{-6}. Each result is linked to model and spectrum hashes. For the three baselines, six search patterns and one manual single-pixel pattern evaluated with this coarse configuration, the occupancy–J correlation is −0.941. This selected sample indicates a strong association with metal coverage, but does not establish monotonicity: the manual edge-pixel pattern yields a higher exploratory objective than the empty window.

The absorption band near 9.5 µm is consistent with the SiO_2 response [9]. At this wavelength, the stored loss partition for the manual single-pixel case attributes approximately 94% of the calculated absorption to the continuous spacer. Together with the negative occupancy–J correlation, this supports the interpretation that metal coverage limits optical access to the lossy spacer.

Under this exploratory discretization, the empty-window baseline yielded a higher discrete objective than the initial pattern. After two connectivity rejections, the first evaluated search candidate yielded J = 0.0783 with a batch runtime of 2099 s. The completed study comprised 19 suggestions: six physical evaluations, four connectivity rejections and nine duplicate rejections. The summed batch runtime was 2.97 h. Objectives in evaluation order were 0.0783, 0.0694, 0.0688, 0.0656, 0.0692 and 0.0734. None exceeded the initial or empty-window baseline, and the startup sample remained the best search candidate. The history demonstrates candidate evaluation, screening and persistent objective updates within a fixed budget.

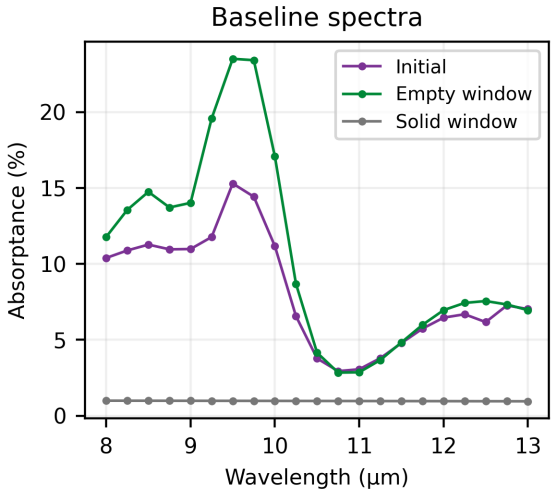


Figure 4. Absorptance spectra of the initial, empty-window and solid-window baselines at h = 1.5 µm. All models retain the fixed frame.

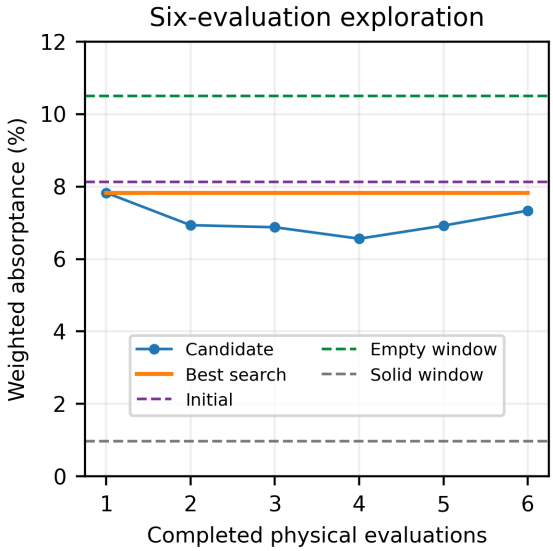


Figure 5. Candidate objectives and best-so-far values for six completed evaluations with seed 42. Horizontal lines indicate the three baseline objectives.

5.3 Repeatability and discussion

A same-machine repeat of the empty-window evaluation changed J by 1.72×10^{-15}. The replay through the corrected controller yielded $J \approx 0.105065$. The relative objective difference from the archive was 3.88×10^{-13}, and the maximum absolute pointwise difference in A was 3.44×10^{-13}. Reconstruction from MATLAB source, without loading the archived .mph file, reproduced the 10.5 μm response with a relative difference in A below 1.5×10^{-13}. These comparisons establish same-machine repeatability of model preparation, solution and extraction; they do not measure physical accuracy.

Numerical sensitivity tests separately assess accuracy. For the empty window, changing the rational-PML scaling factor produced a relative difference in A of 1.187% and absolute differences in R and T of 0.003573 and 0.002759, respectively, exceeding the specified limits. For the initial pattern at 10.5 μm, refinement from h = 1.0 to 0.75 μm changed A by 0.845%, while absolute changes in R and T of 0.001775 and 0.00145 exceeded the 0.001 limits. Both relative A changes use the cmp denominator defined in Section 3. The patterned configuration therefore fails the mesh and PML acceptance criteria despite passing power checks and exhibiting repeatability. Selected polynomial-PML comparisons characterize alternative settings without establishing acceptance of the original spectra.

A manual edge-pixel candidate yielded $J \approx 0.109796$, compared with $J \approx 0.105607$ for the empty window, at h = 1.0 μm with 20-layer polynomial PMLs and otherwise identical numerical settings. This provisional 3.97% increase was obtained separately from the TPE study. A two-wavelength comparison between h = 1.5 and 1.0 μm with the same polynomial PMLs failed the R-change criterion at 9.5 μm ($|\Delta R| = 1.17\times10^{-3} > 0.001$). A separate local-refinement check from the h = 1.0 μm setting passed at those two wavelengths, but does not establish global or full-band accuracy; the objective remains provisional.

Spectral sampling also limits interpretation. At 9.625 μm, the empty-window absorptance exceeds linear interpolation between adjacent grid points by 0.00744. The 12.5 μm sample lies only 0.0220 μm from an air-side diffraction threshold. The reported J therefore remains a prescribed discrete objective; the original grid does not establish peak resolution or convergence over the continuous band.

The transferable elements are the links among candidate parameters, model settings, spectra and objectives, together with separate records of run-level screening and numerical tests. In other parameterized COMSOL models, these records can support replay, duplicate detection and identification of settings associated with failed checks. Each application requires appropriate observables, reference solutions and tolerances. The present case demonstrates these mechanisms for normally incident x-polarized illumination. Uniform-layer agreement does not validate patterned diffraction channels, and same-machine replay does not establish cross-machine reproducibility. Experimental device performance, unpolarized response and optimizer superiority remain outside the scope of this study.

6. Conclusions

The COMSOL and Optuna workflow links binary patterns to their models, spectra and objectives and screens each run before recording an exploratory score. Independent uniform-layer references verify reflection, absorption and substantial transmission. Three baselines, six search evaluations and same-machine reconstruction demonstrate execution and repeatability. The stored history revealed a duplicate-handling defect; its correction was tested in software and exercised through a complete baseline replay. No search candidate exceeded the initial or empty-window baseline, and the patterned spectra failed mesh/PML acceptance criteria. The workflow supports traceable simulation studies and same-machine repeatability while retaining separate numerical acceptance requirements for physical conclusions.

References

[1] A. Y. Piggott, J. Petykiewicz, L. Su, and J. Vučković, “Fabrication-constrained nanophotonic inverse design” [J]. Scientific Reports, 7, 1786 (2017). DOI.
[2] Z. Lin, V. Liu, R. Pestourie, and S. G. Johnson, “Topology optimization of freeform large-area metasurfaces” [J]. Optics Express, 27, 15765–15775 (2019). DOI.
[3] F. F. Qin, Z. Z. Liu, Q. Zhang, H. Zhang, and J. J. Xiao, “Mantle Cloaks Based on the Frequency Selective Metasurfaces Designed by Bayesian Optimization” [J]. Scientific Reports, 8, 14033 (2018). DOI.
[4] J. Bergstra and Y. Bengio, “Random Search for Hyper-Parameter Optimization” [J]. Journal of Machine Learning Research, 13, 281–305 (2012). Online.
[5] T. Pasquier et al., “If these data could talk” [J]. Scientific Data, 4, 170114 (2017). DOI.
[6] G. Bao, Z. Chen, and H. Wu, “Adaptive finite-element method for diffraction gratings” [J]. Journal of the Optical Society of America A, 22, 1106–1114 (2005). DOI.
[7] R. L. Olmon et al., “Optical dielectric function of gold” [J]. Physical Review B, 86, 235147 (2012). DOI.
[8] A. D. Rakić et al., “Optical properties of metallic films for vertical-cavity optoelectronic devices” [J]. Applied Optics, 37, 5271–5283 (1998). DOI.

[9] J. Kischkat et al., “Mid-infrared optical properties of thin films of aluminum oxide, titanium dioxide, silicon dioxide, aluminum nitride, and silicon nitride” [J]. Applied Optics, 51, 6789–6798 (2012). DOI.
[10] D. Chandler-Horowitz and P. M. Amirtharaj, “High-accuracy, midinfrared (450 cm−1 ≤ ω ≤ 4000 cm−1) refractive index values of silicon” [J]. Journal of Applied Physics, 97, 123526 (2005). DOI.
[11] COMSOL AB. Wave Optics Module User’s Guide, version 6.2 [M]. 2023. Online.
[12] M. N. Polyanskiy, “Refractiveindex.info database of optical constants” [J]. Scientific Data, 11, 94 (2024). DOI.
[13] J.-P. Bérenger. A perfectly matched layer for the absorption of electromagnetic waves [J]. Journal of Computational Physics, 114, 185–200 (1994). DOI.
[14] T. Akiba, S. Sano, T. Yanase, T. Ohta, and M. Koyama. Optuna: A Next-generation Hyperparameter Optimization Framework [C]. Proceedings of KDD, 2019: 2623–2631. DOI.
[15] Optuna developers. Optuna 4.1.0 documentation [EB/OL], “optuna.samplers.TPESampler.” Accessed 4 October 2026. Online.
[16] J. S. Bergstra, R. Bardenet, Y. Bengio, and B. Kégl, “Algorithms for Hyper-Parameter Optimization” [C]. Advances in Neural Information Processing Systems, 24 (2011). Online.